

Depressurization of CO₂-rich mixtures in pipes: Two-phase flow modelling and comparison with experiments

Svend Tollak Munkejord*, Morten Hammer

SINTEF Energy Research, P.O. Box 4761 Sluppen, NO-7465 Trondheim, Norway

Abstract

We present and discuss two-phase flow models to simulate transient flow of CO₂-rich mixtures in pipes, which is of relevance for design, operation and safety. The model predictions are compared to data from five depressurization experiments from three facilities. Two flow-model formulations are considered. One is a homogeneous equilibrium model in which the phases travel at the same velocity. The other is a more complex two-fluid model in which the slip between the phases is modelled. The thermodynamic equilibrium of the multi-component mixture, constrained by energy and volume, is computed simultaneously with the flow equations.

In general, good agreement with the experiments is obtained, including the dry-out point where the liquid in the pipe has evaporated. For the friction and heat-transfer models tested, the two-fluid model did not provide substantially better predictions than the homogeneous equilibrium model. The effect of different heat-transfer models is also discussed. In our case, it is necessary to take the pipe heat capacity into account.

Keywords: carbon dioxide, CO₂ transport, pipeline, transient simulation, CFD, fluid dynamics, thermodynamics, depressurization

Nomenclature

Latin letters

c	Speed of sound	m s^{-1}
c_p	Specific heat capacity at constant pressure	$\text{J kg}^{-1} \text{K}^{-1}$
d	Diameter	m
e	Specific internal energy	J kg^{-1}
\tilde{e}	Specific molar internal energy, Sec. 2.4	J mol^{-1}
E	Total energy	J m^{-3}
f	(Darcy) friction factor, see (18)–(21)	–
\mathcal{F}	Friction force	N m^{-3}
\tilde{g}	Specific Gibbs free energy	J mol^{-1}
g_x	Gravitational acceleration in x direction	m s^{-2}
h	Heat-transfer coefficient, Sec. 2.6	$\text{W m}^{-2} \text{K}^{-1}$
h	Specific enthalpy, Sec. 2.7	J kg^{-1}
\tilde{h}	Specific molar enthalpy, Sec. 2.4	J mol^{-1}

*Corresponding author.

Email address: [svend.t.munkejord \[a\] sintef.no](mailto:svend.t.munkejord@ Sintef.no) (Svend Tollak Munkejord)

\dot{m}	Mass flux	$\text{kg m}^{-2} \text{s}^{-1}$
n	Time step	-
\tilde{n}	Composition vector	mol mol^{-1}
Nu	Nusselt number	-
P	Pressure	Pa
Pr	Prandtl number	-
q	Heat flux	W m^{-2}
Q	Heat	W m^{-3}
r	Radius	m
R	Universal gas constant	$\text{J mol}^{-1} \text{K}^{-1}$
Re	Reynolds number	-
\tilde{s}	Specific molar entropy, Sec. 2.4	$\text{J mol}^{-1} \text{K}^{-1}$
t	Time	s
T	Temperature	K
u	Velocity	m s^{-1}
\tilde{v}	Specific molar volume, Sec. 2.4	$\text{m}^3 \text{mol}^{-1}$
W	State function	J mol^{-1}
x	Spatial coordinate	m
z	Mass fraction	kg kg^{-1}
Z	Compressibility factor	-

Greek letters

α	Volume fraction	$\text{m}^3 \text{m}^{-3}$
δ	Factor in (12)	-
λ	Thermal conductivity	$\text{W m}^{-1} \text{K}^{-1}$
μ	Dynamic viscosity	$\text{kg m}^{-1} \text{s}^{-1}$
Ψ	Mass-transfer, see (10)	$\text{kg m}^{-3} \text{s}^{-1}$
ϕ_i	Interfacial momentum exchange	N m^{-3}
Φ	Coefficient in (18)	-
ρ	(Mass) density	kg m^{-3}

Subscripts

amb	Ambient condition
B	Bernoulli, Sec. 2.7
c	Choke
f	Fluid
g	Gas
i	Interfacial or inner or initial
j	Component
k	Phase k
ℓ	Liquid
min	Minimum
o	Outer
R	Riemann, Sec. 2.7
spec	Specified condition
w	Wall

Abbreviations

BBC	Bernoulli-choking-pressure boundary condition, Sec. 2.7
BC	Boundary condition
C	Colburn
CBC	Characteristic-based boundary condition, Sec. 2.7

CCS	CO ₂ capture & storage
CFL	Courant–Friedrichs–Lewy
EOS	Equation of state
FORCE	First-order centred
GERG	Groupe européen de recherches gazières
GW	Gungor–Winterton
HEM	Homogeneous equilibrium model
MUSTA	Multistage centred
PR	Peng–Robinson
TFM	Two-fluid model

1. Introduction

Large-scale deployment of CCS (CO₂ capture & storage) will require transport of large quantities of CO₂ from the points of capture to the storage sites. A major part will probably be handled in pipeline networks. CO₂ transport by pipeline differs from e.g. that of natural gas in a number of ways. First, the CO₂ will normally be in a liquid or dense liquid state, while the natural gas most often is in a dense gaseous state, see e.g. Aursand *et al.* (2013). Next, depending on the capture technology, the CO₂ will contain various impurities (NETL, 2013), which may, even in small quantities, significantly affect the thermophysical properties (Li *et al.*, 2011a,b), which, in turn, affect the depressurization and flow behaviour (Munkejord *et al.*, 2010).

Although CO₂ has been transported by pipeline for the purpose of enhanced oil recovery (US DOE, 2010), mainly in the USA, the CCS case will likely be different, due to the different impurities, and due to the proximity, in many cases, to densely populated areas. As a result of this, and because of the expected scale of CCS (IEA, 2014), it will be of importance to design and operate CO₂ pipelines in an economical and safe way.

It has been found that a pipeline transporting CO₂ will be more susceptible to running-ductile fracture than one carrying natural gas (Mahgerefteh *et al.*, 2012; Aursand *et al.*, 2014). One part of the design to avoid running-ductile fracture necessitates accurate models predicting the depressurization behaviour of the relevant CO₂-rich mixtures, noting that existing semi-empirical models have been deemed not to be directly applicable to CO₂ pipelines (Jones *et al.*, 2013). In this respect, the development of coupled fluid-structure models containing more physics (Aihara and Misawa, 2010; Mahgerefteh *et al.*, 2012; Nordhagen *et al.*, 2012) may lead to a better predictive capability. Furthermore, even though the CO₂ pipeline is primarily designed to operate in the single-phase region, two-phase flow may occur. This may be due to fluctuating CO₂ supply (Klinkby *et al.*, 2011) or during transient events, such as start-up, shut-in or depressurization (Munkejord *et al.*, 2013; Hetland *et al.*, 2014). During depressurization, low temperatures may be attained. It is of interest to have good estimates of these temperatures, since pipeline materials have a minimum temperature at which they lose toughness.

The computation of near-field dispersion of CO₂ from a leaking pipeline forms part of quantified risk analysis and entails the 2D or 3D modelling of the expanding CO₂ jet, see e.g. Wareing *et al.* (2014). However, such computations require a description of the CO₂ state at the puncture or rupture of the pipe. One suitable way to do this is to employ a pipe-flow model.

The above issues call for the development of engineering tools accurately predicting the single- and two-phase flow of CO₂-rich mixtures in pipes. The present work

represents one step in this direction. The published literature containing relevant CO₂-flow data has been scarce, but recently, some depressurization experiments with pure CO₂ and with CO₂-rich mixtures have been published. Depressurization experiments are interesting for two reasons. First, the pressure-wave propagation during depressurization is interesting in itself, due to its application to fracture-propagation control. Second, the flow-model formulation has inherent wave-propagation velocities, which ought to agree with the experimental observations. This may be challenging in the two-phase region.

Drescher *et al.* (2014) presented experiments and simulations for depressurization of three CO₂-N₂ mixtures. The N₂ content in the three experiments was 10, 20 and 30 mol %. The initial conditions for the experiments were approximately 12.0 MPa and 20 °C for all cases. The tube used was about 140 m long and the internal diameter was 10.0 mm. The logging rate of the pressure was 5 kHz for the initial 10 s, thereafter 100 Hz. Simulations were performed using a homogeneous equilibrium model (HEM), and good agreement with the experiments was obtained for the pressure. Comparison between simulated and measured temperature indicated, among other things, slow temperature sensors.

Botros *et al.* (2013) presented an experiment with a mixture of 72.6 mol % CO₂ and 27.4 mol % CH₄, representing gas used for enhanced oil recovery. A specialized high-pressure shock tube (42 m long, and 38.1 mm internal diameter) was used. The inner pipe wall was honed to get a smooth surface, with very little friction, to better resemble larger industrial pipes. The experiment was conducted with a very high initial pressure of 28.568 MPa, and a high initial temperature of 40.5 °C. Botros *et al.* employed high-frequency response dynamic-pressure transducers, with a logging rate up to 20 kHz. The shock-tubes and experiments were designed to measure and study the decompression wave speed, the velocity of the rarefaction wave propagating into the pipeline, after rupture of a burst disc.

National Grid (Cosham *et al.*, 2012) have conducted 14 shock-tube experiments from dense/liquid phase pure CO₂ and CO₂-rich mixtures with impurities (H₂, N₂, O₂, CH₄). The pipeline segment used was 144 m long and had an internal diameter of 146.36 mm. One of the mixture experiments, CO₂-H₂-N₂-O₂-CH₄, was presented in more detail, and the pressure levels for the initial 50 ms were plotted. Pressure was sampled at a frequency of 100 kHz. The motivation for performing the shock-tube experiments was to improve the understanding of CO₂ and CO₂-mixture decompression behaviour, in order to predict the pipe material toughness required to arrest a running-ductile fracture. The initial conditions ranged from 3.89 MPa to 15.4 MPa and from 0.1 °C to 35.6 °C.

The CO₂-H₂-N₂-O₂-CH₄ experiment of Cosham *et al.* (2012), and the Botros *et al.* (2013) experiment, were compared to numerical simulations by Elshahomi *et al.* (2015). They used a finite-volume approach in ANSYS Fluent, and discretization of the pipe in 2D axial symmetry. The Advection Upstream Splitting Method of Liou and Steffen (1993) was employed for the inter-cell flux calculations. For the thermodynamic closure, Elshahomi *et al.* used the GERG-2008 equation of state (EOS) (Kunz and Wagner, 2012).

Data from Cosham *et al.* (2012), including the CO₂-H₂-N₂-O₂-CH₄ experiment, were also considered by Jie *et al.* (2012), who employed a semi-implicit numerical method to solve the HEM (Xu *et al.*, 2014) with the Peng–Robinson–Stryjek–Vera EOS (Stryjek and Vera, 1986).

For the case of pure CO₂, Brown *et al.* (2014) compared a homogeneous equilibrium model and a two-fluid model (TFM) with a formulation similar to that of Paillère *et al.* (2003), to depressurization experiments. Both chemical potential and temperature were

relaxed, while the pressure of the two phases was identical. The experiments were conducted in a straight 260 m long pipe with an internal diameter of 233 mm. Better agreement between the experiments and the TFM was observed, than for the HEM.

In this work, we consider multicomponent CO₂ mixtures and discuss two formulations of the flow model. The first is a HEM while the second is a TFM. We discuss the performance of the models comparing with data from five different full-bore pressure-release experiment from three different facilities (Botros *et al.*, 2013; Cosham *et al.*, 2012; Drescher *et al.*, 2014). The data from the two first facilities are pressure data from the first part of the depressurization. The data from the latter facility are pressure and temperature data taken over a longer time span, such that wall friction, interphasic friction and heat transfer are expected to play a significant role. In particular, the data and simulations include the dry-out point, i.e., the point at which all the liquid has evaporated. Dry-out is challenging to model, since it is sensitive to both the flow-model formulation and the employed closure relations.

In our compressible two-phase flow models, full thermodynamic equilibrium (pressure, temperature and chemical potential) is assumed. With this assumption, the iso-choric–iso-energetic phase-equilibrium problem must be solved, unless modelling simplifications are made. When engineering equations of state are required, this is a challenging and CPU-demanding problem. As a consequence, computational fluid dynamics (CFD) simulations with advanced EOSs are commonly performed using tabulated thermodynamic state variables and fluid phase properties (Elshahomi *et al.*, 2015; Pini *et al.*, 2015; Swesty, 1996; Timmes and Swesty, 2000; Xia *et al.*, 2007; Kunick *et al.*, 2008). Thermodynamic consistency of the tabulated approximation is rarely addressed, even though this might lead to some entropy production (Swesty, 1996). For single-component fluids, there are some examples of finite-volume simulations where engineering EOSs are solved directly, without tabulation prior to the simulation (Giljarhus *et al.*, 2012; Hammer *et al.*, 2013; Hammer and Morin, 2014; Brown *et al.*, 2014). Michelsen (1999) describes a framework for solving the multi-component iso-choric–iso-energetic phase equilibrium that guarantees a solution. In this work, the methods of Michelsen have been adapted and used for the Peng and Robinson (1976) (PR) EOS. For more CPU-demanding EOSs, like the multi-component reference EOS GERG-2008 (Kunz and Wagner, 2012) or EOS-CG (Gernert and Span, 2010), practical implementations are likely required to use property tabulation. EOS-CG is similar to GERG-2008, but the component interaction parameters are tuned to match the properties of CO₂-rich systems. Different Helmholtz mixture rules are also used for some components. EOS-CG is under development, and currently, only a limited set of impurities are supported.

The rest of this article is organized as follows: Section 2 briefly presents the formulation of the homogeneous equilibrium model and the two-fluid model, the employed models for thermophysical properties, as well as the constitutive models for friction and heat transfer. Model predictions are compared to experiments and discussed in Section 3. Conclusions are drawn in Section 4.

2. Models

In this work, we model the pipeflow as one-dimensional. The flow can be single-phase or two-phase gas-liquid. The gas and the liquid consist of multiple chemical components. Gravity, friction and heat transfer to the surroundings are accounted for by source terms. Viscous effects other than wall or interphasic friction are ignored. Full thermodynamical equilibrium is assumed, i.e., the phases have the same pressure,

temperature and chemical potential. We consider two flow models, described in the following. The first is a drift-flux model with no slip, or a homogeneous equilibrium model. The second is a more complex two-fluid model, in which the interphasic friction is explicitly modelled. For a mathematical background of two-phase flow modelling, see e.g. Drew (1983).

2.1. Homogeneous equilibrium model

In the homogeneous equilibrium model (HEM), it is assumed that the phases travel with the same velocity. The governing equations will then have the same form as the Euler equations for single-phase compressible inviscid flow, and consist of a mass-conservation equation,

$$\frac{\partial}{\partial t}(\rho) + \frac{\partial}{\partial x}(\rho u) = 0, \quad (1)$$

a momentum-balance equation,

$$\frac{\partial}{\partial t}(\rho u) + \frac{\partial}{\partial x}(\rho u^2 + P) = \rho g_x - \mathcal{F}_w, \quad (2)$$

and a balance equation for the total energy,

$$\frac{\partial}{\partial t}(E) + \frac{\partial}{\partial x}u(E + P) = \rho g_x u + Q. \quad (3)$$

Herein, $\rho = \alpha_g \rho_g + \alpha_\ell \rho_\ell$ is the density of the gas (g) and liquid (ℓ) mixture. u is the common velocity and P is the pressure. $E = \rho(e + 1/2u^2)$ is the total energy of the mixture, while $e = (e_g \alpha_g \rho_g + e_\ell \alpha_\ell \rho_\ell) / \rho$ is the mixture specific internal energy. α_k denotes the volume fraction of phase $k \in \text{g}, \ell$. \mathcal{F}_w is the wall friction and Q is the heat transferred through the pipe wall. g_x is the gravitational acceleration in the axial direction of the pipe.

2.2. Two-fluid model

In the two-fluid model (TFM), the phases may travel with different velocities. As a result of this, the chemical composition may change along the pipe. We therefore solve a mass-conservation equation for each chemical component in the gas, as well as in the liquid:

$$\frac{\partial}{\partial t}(\alpha_g \rho_g z_{g,j}) + \frac{\partial}{\partial x}(\alpha_g \rho_g z_{g,j} u_g) = \Psi_{g,j}, \quad (4)$$

$$\frac{\partial}{\partial t}(\alpha_\ell \rho_\ell z_{\ell,j}) + \frac{\partial}{\partial x}(\alpha_\ell \rho_\ell z_{\ell,j} u_\ell) = \Psi_{\ell,j}. \quad (5)$$

The model further consists of a momentum-balance equation for each phase,

$$\frac{\partial}{\partial t}(\alpha_g \rho_g u_g) + \frac{\partial}{\partial x}(\alpha_g \rho_g u_g^2) + \alpha_g \frac{\partial P}{\partial x} + \phi_i = u_i \Psi + \alpha_g \rho_g g_x - \mathcal{F}_{wg}, \quad (6)$$

$$\frac{\partial}{\partial t}(\alpha_\ell \rho_\ell u_\ell) + \frac{\partial}{\partial x}(\alpha_\ell \rho_\ell u_\ell^2) + \alpha_\ell \frac{\partial P}{\partial x} - \phi_i = -u_i \Psi + \alpha_\ell \rho_\ell g_x - \mathcal{F}_{w\ell}, \quad (7)$$

and a total-energy-balance equation for the gas-liquid mixture,

$$\frac{\partial}{\partial t}(E_g + E_\ell) + \frac{\partial}{\partial x}(E_g u_g + \alpha_g u_g P) + \frac{\partial}{\partial x}(E_\ell u_\ell + \alpha_\ell u_\ell P) = \alpha_g \rho_g g_x u_g + \alpha_\ell \rho_\ell g_x u_\ell. \quad (8)$$

Herein, $E_k = \rho_k(e_k + 1/2u_k^2)$ is the total energy of phase k . $u_i = 1/2(u_g + u_\ell)$ is the interfacial momentum velocity. Morin and Flåtten (2012) showed that this choice of interfacial momentum velocity does not produce entropy, and Hammer and Morin (2014) further showed that it preserves the kinetic energy for the system. The volume fractions satisfy

$$\alpha_g + \alpha_\ell = 1. \quad (9)$$

$\Psi_{k,j}$ is the mass transfer to chemical component j in phase k . Since mass is conserved, we have

$$\Psi = \sum_j \Psi_{g,j} = - \sum_j \Psi_{\ell,j}. \quad (10)$$

The mass transfer is calculated at each time step using an instantaneous relaxation procedure analogous to the one described by Hammer and Morin (2014), imposing full thermodynamic (pressure, temperature and chemical potential) equilibrium. This implies that the conserved mass of gas and liquid must be updated after the relaxation procedure. The characteristic wave-structure of the model (4)–(8) will, due to the instantaneous relaxation, recover the structure of a model with a single mass-conservation equation per component.

ϕ_i denotes the interfacial momentum exchange. Here we employ the model

$$\phi_i = \Delta P_i \frac{\partial \alpha_g}{\partial x} + \mathcal{F}_i, \quad (11)$$

where ΔP_i is the difference between the average bulk pressure and the average interfacial pressure. \mathcal{F}_i is an interface friction model treated as a source term. Following earlier works (Stuhmiller, 1977; Bestion, 1990; Munkejord *et al.*, 2009), we take

$$\Delta P_i = \delta \frac{\alpha_g \alpha_\ell \rho_g \rho_\ell}{\alpha_g \rho_\ell + \alpha_\ell \rho_g} (u_g - u_\ell)^2, \quad (12)$$

where $\delta = 1.2$.

2.3. Thermophysical property models

In order to model gas-liquid phase equilibrium, phase densities and energies, we employ the Peng and Robinson (1976) EOS. Classical van der Waals mixing rules and symmetric binary interaction parameters are used. For the ideal heat capacity, correlations from the American Petroleum Institute, research project 44 (1976) are used. The fluid thermal conductivity and dynamic viscosity are calculated using the TRAPP model (Ely and Hanley, 1981, 1983).

2.4. Phase equilibrium

For a numerical flow simulation, phase equilibrium must typically be determined from the given amounts of the components, \mathbf{n} , and additionally two state variables. Depending on the available input we employ one of three methods, listed with increasing complexity of the problem formulation:

- Initial conditions: Pressure (P) and temperature (T) are specified (PT -flash)
- Boundary conditions: Pressure (P) and entropy (\tilde{s}) are specified ($P\tilde{s}$ -flash)
- Conserved variables: Specific molar internal energy (\tilde{e}) and specific molar volume (\tilde{v}) are specified ($\tilde{e}\tilde{v}$ -flash)

The most common phase-equilibrium calculation, the PT -flash, is a global minimization problem for the Gibbs free energy, \tilde{g} , of the system. The difficulty in solving this minimization lies in correctly to determine the number of phases and their composition. For the pressure and temperature range of the mixtures used in this work, it is known that the mixture can only exhibit a single-phase or a two phase, gas-liquid mixture, behaviour. This simplifies the minimization considerably. The two-phase PT -flash is thoroughly studied, and a numerical framework is described in detail by Michelsen and Mollerup (2007).

In the single-phase pressure-temperature region where the equation of state, $P = P(T, \tilde{v}, \tilde{\mathbf{n}})$, only has one density root, it is not possible to distinguish between a gas phase and a liquid phase. In this case, the phase is defined to be liquid, when the compressibility factor, $Z = P\tilde{v}/(RT)$, is less than the pseudo-critical compressibility factor of the mixture (0.3074... for the Peng-Robinson EOS). Otherwise the phase is defined to be gas. R is the universal gas constant.

The $P\tilde{s}$ -flash is a global minimization of enthalpy, \tilde{h} , subject to specifications on pressure, P_{spec} , entropy, \tilde{s}_{spec} , and composition. For multicomponent mixtures, the $P\tilde{s}$ -flash can be transformed to a single-variable unconstrained minimization problem utilizing a state function, W , and the PT -flash in an inner loop (Michelsen, 1999):

$$W(T) = -\tilde{g}_{\min} - T\tilde{s}_{\text{spec}}. \quad (13)$$

Here the result of the PT -flash Gibbs free energy minimization is \tilde{g}_{\min} . Differentiating (13) with respect to T , we obtain

$$\frac{dW}{dT} = \tilde{s}_{\min} - \tilde{s}_{\text{spec}} \quad (14)$$

where \tilde{s}_{\min} is the entropy evaluated at the Gibbs free energy minimum found by the PT -flash. This shows that the entropy constraint is satisfied at the stationary point of the minimization.

The $\tilde{e}\tilde{v}$ -flash, or iso-choric-iso-energetic phase equilibrium problem, is a global minimization of entropy with constraints on internal energy, \tilde{e}_{spec} , specific volume, \tilde{v}_{spec} , and composition. In a similar manner, a state function can be used to transform the constrained minimization to an unconstrained problem,

$$W(T, P) = -\frac{(\tilde{g}_{\min} - \tilde{e}_{\text{spec}} - P\tilde{v}_{\text{spec}})}{T}. \quad (15)$$

Again the stationary point found by differentiating (15) satisfies the constraints on internal energy and specific volume,

$$\frac{\partial W}{\partial T} = \frac{(\tilde{h}_{\min} - \tilde{e}_{\text{spec}} - P\tilde{v}_{\text{spec}})}{T^2}, \quad (16)$$

$$\frac{\partial W}{\partial P} = -\frac{(\tilde{v}_{\min} - \tilde{v}_{\text{spec}})}{T}, \quad (17)$$

where \tilde{h}_{\min} is the enthalpy evaluated at the Gibbs free energy minimum found by the PT -flash.

In order to get a properly scaled Hessian matrix, $\ln T$ and $\ln P$ are used as variables instead of T and P . This nested-loop approach is CPU demanding compared to solving the full set of equilibrium conditions simultaneously, but guarantees convergence. At the same time, good initial values are available from the previous time step. The approach for solving the full equilibrium equation set described by Michelsen (1999) is used in this work, and the nested-loop approach is used as a fail-safe alternative.

2.5. Friction models

The wall friction for the homogeneous equilibrium model is calculated as

$$\mathcal{F}_w = \begin{cases} f_k \frac{\dot{m}|\dot{m}|}{2\rho_k d_i} & \text{for single-phase flow} \\ f_\ell \frac{\dot{m}|\dot{m}|}{2\rho_\ell d_i} \Phi & \text{for two-phase flow,} \end{cases} \quad (18)$$

where $f_k = f(Re_k)$ is the Darcy friction factor, $Re_k = |\dot{m}|d_i/\mu_k$ is the Reynolds number for phase k and $\dot{m} = \rho u$ is the mass flux. The coefficient Φ is an empirical correlation, which is used to account for two-phase flow, and depends on various properties of both phases. Here we have employed the Friedel (1979) correlation. Details of the calculation of the two-phase coefficient Φ , and also further discussion, can be found in Aakenes (2012); Aakenes *et al.* (2014).

The friction terms for the two-fluid model, \mathcal{F}_{wg} , $\mathcal{F}_{w\ell}$ and \mathcal{F}_i , are calculated using the model of Spedding and Hand (1997), developed for co-current stratified flow. For pipe depressurizations, this is believed to be a reasonable assumption some way away from the pipe outlet. The corresponding shear stresses, τ , for wall-gas, wall-liquid and the gas-liquid interface, are calculated as

$$\tau_{wg} = f_{wg} \frac{\rho_g u_g^2}{2}, \quad (19)$$

$$\tau_{w\ell} = f_{w\ell} \frac{\rho_\ell u_\ell^2}{2}, \quad (20)$$

$$\tau_i = f_i \rho_g \frac{(u_g - u_\ell)^2}{2}. \quad (21)$$

Here, wall-gas, f_{wg} , wall-liquid, $f_{w\ell}$, and gas-liquid, f_i , interfacial friction factors are calculated from Reynolds-number-based correlations. Shear stresses and friction are related by contact perimeter and pipe area.

2.6. Heat-transfer model

Since in this work we consider cylindrical tubes whose length is far greater than the thickness, we assume axisymmetry along the tube axis and neglect axial conduction. If the tube has a negligible heat capacity, the radial temperature profile will be in steady state, and the heat-transfer term can be modelled as

$$Q = \frac{T_o - T}{\frac{r_i}{h_i} + \frac{r_i^2}{r_o} + \frac{r_i^2 \ln(r_o/r_i)}{\lambda}}, \quad (22)$$

where r_i and r_o are the tube inner and outer diameter, respectively. T is the fluid temperature and T_o is the surrounding temperature. h_i and h_o are the inner and outer heat-transfer coefficient, and λ is the tube thermal conductivity.

In some cases, the tube has a significant heat capacity, which invalidates the assumption of a steady-state radial temperature. One then needs to solve the heat equation

$$\rho c_p \frac{\partial T}{\partial t} - \frac{1}{r} \frac{\partial}{\partial r} \left(\lambda r \frac{\partial T}{\partial r} \right) = 0 \quad (23)$$

along with the flow model, assuming radial symmetry and that axial conduction can be neglected. Herein, c_p is the specific heat capacity of the tube material.

To calculate the inner heat-transfer coefficient, h_i , two correlations are implemented. The first is a simple Nusselt-number, Nu , correlation,

$$Nu = \begin{cases} 3.66 & Re < 2300, \\ 0.023Re^{4/5}Pr^{1/3} & Re > 3000, \end{cases} \quad (24)$$

with linear interpolation in the region $2300 \leq Re \leq 3000$. The second line is the Colburn correlation, see e.g. Bejan (1993, Chap. 6). The Nusselt number, Nu , and the Prandtl number, Pr , are defined as

$$Nu = \frac{h_i d_i}{\lambda_f}, \quad Pr = \frac{c_{p,f} \mu_f}{\lambda_f}, \quad (25)$$

where subscript f indicates fluid (mixture) properties.

To account for the enhanced heat transfer due to boiling, the correlation of Gungor and Winterton (1987) is chosen for its simplicity. The heat flux, q (W m^{-2}), correlation is implicitly formulated,

$$q = q(h_i(q), T_w, T). \quad (26)$$

We calculate the heat-transfer coefficient in an explicit manner based on the fluid solution at time step n and the heat flux from time step $n - 1$.

2.7. Outlet boundary condition

The method for setting outlet boundary conditions for hyperbolic systems should, strictly speaking, be based on the incoming characteristics at the outlet, see e.g. Munkejord (2006) for an example regarding a two-fluid model. Often, however, simpler boundary conditions work well enough in practice. Nevertheless, we find it appropriate briefly to discuss the implementation and effect of the outlet boundary conditions.

In this work, the boundary conditions (BCs) are implemented using one ghost cell. The boundary conditions are applied at each time step of the simulation. We have tested three different methods. The simplest, which we will refer to as the ‘pressure BC’ consists of setting the pressure in the ghost cell according to the following formula:

$$P_o(t) = \begin{cases} P_{\text{amb}} + (P_i - P_{\text{amb}}) \cos\left(\frac{\pi t}{2t_\delta}\right) & 0 \leq t < t_\delta, \\ P_{\text{amb}} & t \geq t_\delta. \end{cases} \quad (27)$$

Herein, P_i is the initial tube pressure and P_{amb} is the ambient pressure. The cosine term is employed to model slow-opening valves, where t_δ is the valve-opening time. By default, we assume infinitely fast rupture discs, i.e., $t_\delta = 0$.

The mixture entropy, mixture composition and phasic velocities are extrapolated to the ghost cell. The state in the ghost cell (including temperature) is then calculated using these variables and the set pressure from (27). Due to the nature of the flow equations, even this simple BC method often gives good results in practice. This is further discussed in Section 3.3.1.

The flow state at the outlet will often be choked, or sonic. A refined BC method consists of considering the choking pressure, P_c . It can be found by integrating a Riemann invariant from the last cell of the domain, and locating the pressure where the flow becomes sonic. For a given entropy and composition, the relevant HEM Riemann invariant can be expressed as follows,

$$u_R(P) = u_i - \int_{P_i}^P \frac{dP}{\rho(P)c(P)}. \quad (28)$$

Herein, subscript i denotes the state in the last cell in the inner domain. In order to find the choking pressure, the equation $u_R(P_c) = c(P_c)$ must be solved for P_c . We then set

$$P_{\text{CBC}} = \max(P_c, P_o) \quad (29)$$

as a boundary condition. This can be viewed as a characteristic-based BC and it will be referred to as CBC.

In general, the equation (28) must be integrated numerically. As a simpler alternative, the choking pressure can be estimated using a steady-state flow assumption, and applying the Bernoulli equation,

$$\frac{1}{2} (u_B(P))^2 + h(P) = \frac{1}{2} u_i^2 + h_i. \quad (30)$$

Constant mixture entropy and composition are assumed. In this case, the choking pressure is found by solving $u_B(P'_c) = c(P'_c)$ for the estimated choke pressure, P'_c . The Bernoulli choking pressure is applied in the same manner as the Riemann choking pressure,

$$P_{\text{BBC}} = \max(P'_c, P_o). \quad (31)$$

The use of the Bernoulli choking pressure as a boundary condition will be referred to as BBC.

2.8. Numerical methods

The fluid-dynamical models of Sections 2.1 and 2.2 are integrated in space and time using the finite-volume method with the FORCE flux (Toro and Billett, 2000). In our experience, it is a very robust method. It is also optimal in the sense that it has the least numerical dissipation of the first-order central schemes that are stable for all Courant–Friedrichs–Lewy (CFL) numbers less than unity (Chen and Toro, 2004). FORCE is the building-block of the multistage centred (MUSTA) scheme of Toro (2006); Titarev and Toro (2005), which we have also employed for two-phase flow models (Munkejord *et al.*, 2006). However, for cases involving phase change, we have found that the additional robustness of the FORCE scheme is sometimes required. Regarding the two-fluid model of Section 2.2, the non-conservative terms have been discretized similarly to the approach of Munkejord *et al.* (2009); Hammer and Morin (2014). For the cases presented in the following, a CFL number of 0.85 has been employed. We employ a regular cell-centred grid. The required grid sizes have been found by grid-dependence studies for each case, see Figure 8a for an example. For all the cases, a grid density of about 10 cells per metre gave accurate numerical results. For Case 2, however, a finer grid was required to capture the pressure-sensor positions.

The heat equation (23) is also solved employing the finite-volume method with Forward Euler time integration. The time stepping is subject to the stability criterion $\Delta t_{\text{max}} = \rho c_p \Delta r^2 / (2\lambda)$. In the following, we employ a radial grid of 10 cells and use a time-step length of $0.8\Delta t_{\text{max}}$ for the heat equation. Usually the time step is limited by the fluid model.

3. Results and discussion

In the following, we will consider three pipe configurations and five different CO₂-rich mixtures. The initial conditions are given in Table 1 and the mixture compositions in Table 2. The positions at which experimental data are taken, are displayed in Table 3. Cases 1 and 2 focus on the pressure-wave propagation in the initial phase of a depressurization, while Case 3 is a depressurization of longer duration, with both pressure and temperature measurements.

Table 1: Initial conditions of simulated cases.

Mixture #	Pressure (bar)	Temperature (°C)	Ambient temp. (°C)
1	150.5	10.0	
2	285.68	40.5	
3a	119.9	19.5	18.4
3b	120.8	19.7	19.5
3c	120.0	17.3	17.4

Table 2: CO₂-rich mixtures used in this work. Critical point predicted using the PR EOS.

Mixture #	Composition (mol %)					Critical point	
	CO ₂	H ₂	N ₂	O ₂	CH ₄	T (°C)	P (bar)
1	91.03	1.15	4.00	1.87	1.95	25.48	86.1
2	72.6				26.4	7.13	86.39
3a	89.8		10.1			23.45	87.99
3b	80.0		20.0			14.55	104.1
3c	70.0		30.0			3.15	123.8

Table 3: Instrument positions.

Case 1		Case 2		Case 3	
Sensor tag	Position (m)	Sensor tag	Position (m)	Sensor tag	Position (m)
P04	0.34	PT1	0.0295	PT30	0.190
P06	0.54	PT2	0.2	TT30	0.735
P08	0.74	PT3	0.35	PT40	50.690
P10	0.94	PT5	0.7	TT40	51.235
P12	1.24	PT6	0.9	PT50	101.190
P14	1.84	PT7	1.1	TT50	101.735
P16	2.44			PT60	139.190
P18	3.64			TT60	139.950

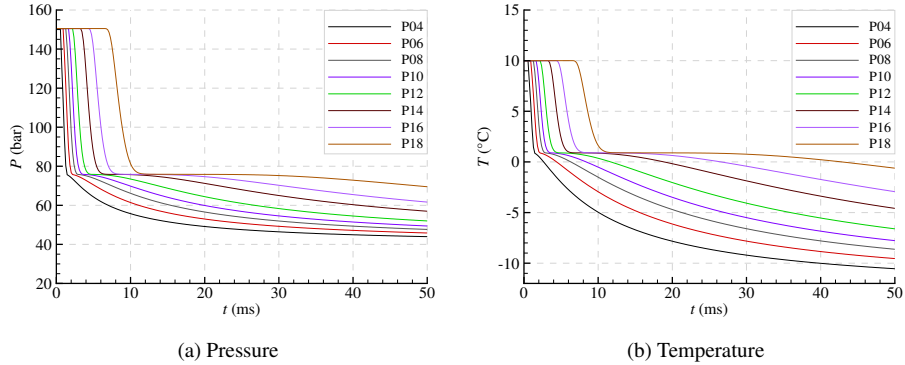


Figure 1: Case 1: Simulated quantities as a function of time at different locations. HEM.

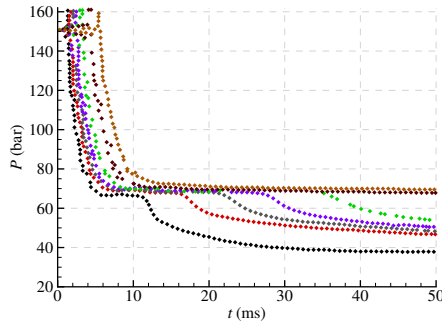


Figure 2: Case 1: Measured pressure. After Cosham *et al.* (2012).

3.1. Case 1: Pressure propagation in a multi-component CO_2 mixture

We will now study the propagation of pressure waves in some detail. First we consider the case published as Test 31 by Cosham *et al.* (2012). A pipe of inner diameter 0.14636 m and length 144 m is filled with a mixture of 91.03 % CO_2 , 1.15 % H_2 , 4.00 % N_2 , 1.87 % O_2 and 1.95 % CH_4 . The percentages are by mol. The initial pressure is 149.5 barg which is about 150.51 bar and the initial temperature is 10.0 °C. At time $t = 0$, the pipe is opened to the atmosphere by the explosive cutting of a rupture disc.

The case was calculated using the HEM. Since we are only interested in the development up to time $t = 50$ ms, it is enough to consider the first 30 m of the pipe. A computational grid of 300 cells was employed. Many of the pressure sensors are close to the open end of the pipe, where the numerical solution is sensitive to the choice of outlet boundary condition. Therefore, we employ the accurate BBC method, described in Section 2.7. Since the simulated time is short, we neglect heat transfer in this case. This is also in line with the approach of Elshahomi *et al.* (2015). The pressure and temperature computed at the positions given by Cosham *et al.* (2012), see Table 3, are plotted as a function of time in Figure 1.

The graph in Figure 1a can be compared with Figure 2, whose data we have extracted from Figure 5 in Cosham *et al.* (2012). There is reasonable agreement between simulation and experiment, with three main points to note. First, the initial drop in pressure was faster in the simulation than in the experiment. We hypothesize that a main reason for this may be that the pipe opens instantaneously in the simulation, while

the opening of the bursting disc may take some time in reality. Second, the measured pressures show plateaux which indicate phase change. These plateaux are longer in the experiment than in the simulation. Third, the measured pressure plateaux show an increasing trend along the pipe. There is no such trend in the simulation.

The graph in Figure 1a may also be compared with Figure 12 in Elshahomi *et al.* (2015). It can be seen that the results are rather similar. This is interesting to note, given the different numerical approaches; Elshahomi *et al.* (2015) employed a 2D model with a different formulation of the outlet boundary conditions, as well as a different equation of state (EOS). The most notable difference is the pressure-plateau level, which is about 76 bar in the present work and about 80 bar in Elshahomi *et al.* (2015). This difference is probably mainly due to the different EOS. We further observe that for this case, Jie *et al.* (2012) calculated a plateau pressure of about 76 bar with their model employing the Peng–Robinson–Stryjek–Vera EOS.

The differences between the presently employed Peng and Robinson (PR) EOS and the GERG-2008 EOS employed by Elshahomi *et al.* (2015) are illustrated in Figure 3. Figure 3a shows the calculated phase envelopes and isentropic decompression paths for the present case. It can be observed that when using the PR EOS, the two-phase area is encountered at a lower pressure, which is consistent with the above observations. Densities are plotted in Figure 3b. The PR EOS is seen to predict too high densities for a given pressure compared to GERG-2008, especially in the upper region of the two-phase area. Figure 3c shows a plot of the speeds of sound. It is seen that the two-phase (mixture) speed of sound predicted by PR and GERG-2008 are not very different, but there is a substantial difference in the single-phase region. The ideal propagation velocity of the rarefaction wave is plotted in Figure 3d. The model differences in the speed of sound are also seen in this plot.

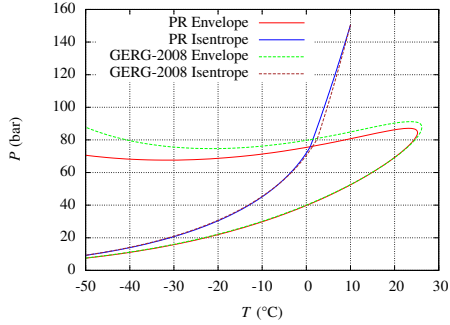
In Figure 4a, the isentropic and HEM depressurization paths for Case 1 are plotted together with the mixture phase envelope. The simulated HEM depressurization path is very close to the ideal isentropic depressurization. This is reasonable, since there is no heat transfer in the HEM simulation, and since the effect of friction is limited.

3.2. Case 2: Pressure propagation with high initial pressure

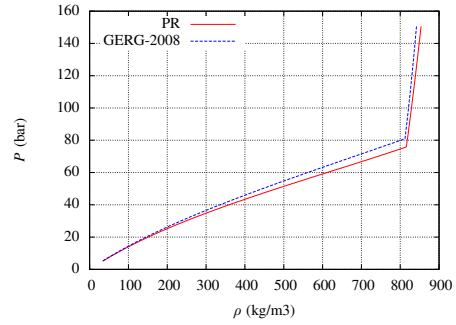
We now consider the case and data published by Botros *et al.* (2013). It consists of a tube of length 42 m and inner diameter 38.1 mm. Further details of the test facility, including sensor positions, are given in Botros (2010). The tube is filled with a mixture consisting of 72.6% CO₂ and 27.4% CH₄ by mol. The initial pressure is rather high, at 285.68 bar, and the initial temperature is also high, at 40.5 °C. At the rupture of a disc at the front end of the tube, a decompression wave propagates up the tube, similarly to the preceding case.

The case has been simulated using the HEM considering the first 15 m of the tube and employing a grid of 2400 cells. A fine grid was required to obtain a good resolution of the sensor positions on our regular grid. The BBC boundary condition, described in Section 2.7, was employed at the outlet.

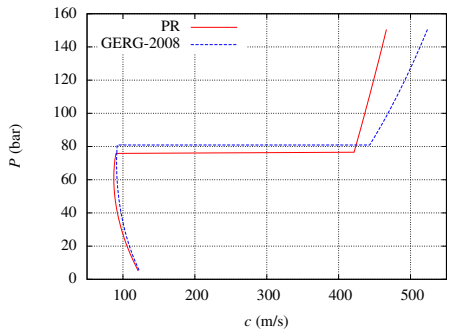
Figure 5a shows simulated and measured pressures plotted at different sensor positions (see Table 3) as a function of time. The corresponding simulated temperatures can be seen in Figure 5b. It can be observed that the simulated pressures drop faster than the measured ones, attaining a lower level. In view of the results of the preceding section, and comparing with the results plotted in Figure 6 of Elshahomi *et al.* (2015), we hypothesize that the main reason for the discrepancy is the EOS. In particular, Figure 5a indicates that the calculated decompression velocity is too low at pressures above



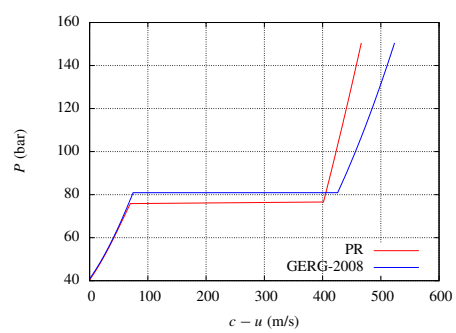
(a) Phase envelope and isentropic depressurization path.



(b) Density along isentropic depressurization path.

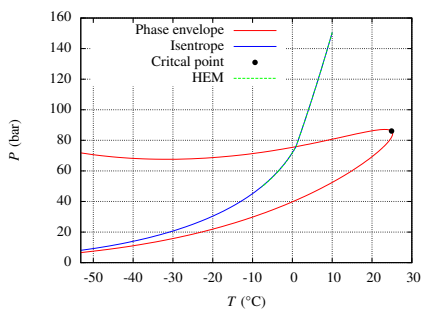


(c) Speed of sound along isentropic depressurization path.

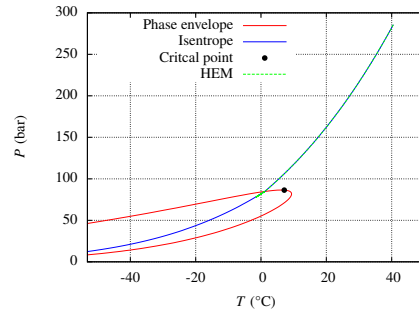


(d) Ideal HEM depressurization velocity.

Figure 3: Comparison of GERG-2008 and PR for the $\text{CO}_2\text{-H}_2\text{-N}_2\text{-O}_2\text{-CH}_4$ mixture (Case 1).



(a) Case 1 ($\text{CO}_2\text{-H}_2\text{-N}_2\text{-O}_2\text{-CH}_4$ mixture). The HEM path is plotted for position P10.



(b) Case 2 ($\text{CO}_2\text{-CH}_4$ mixture). The HEM path is plotted for position PT5.

Figure 4: Phase envelopes plotted for Case 1 ($\text{CO}_2\text{-H}_2\text{-N}_2\text{-O}_2\text{-CH}_4$) and Case 2 ($\text{CO}_2\text{-CH}_4$) together with the isentropic and HEM depressurization paths, from the initial conditions given in Table 1. The critical point is included as a black dot.

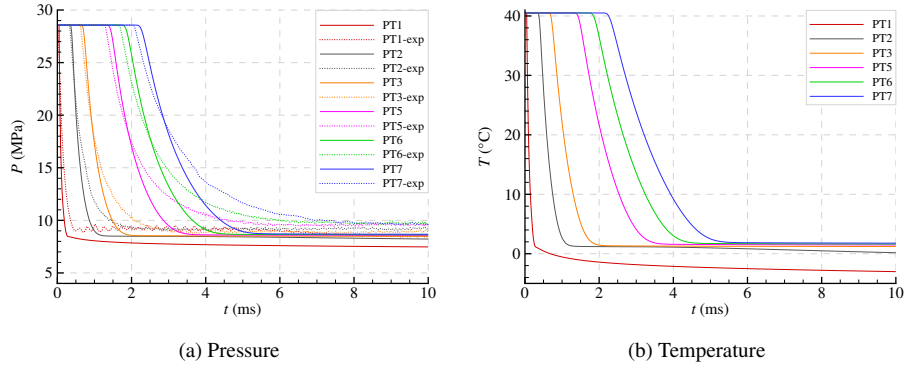


Figure 5: Case 2: Simulated and measured quantities as a function of time at different locations. HEM.

20 MPa, while it is too high below. This is further illustrated in Figure 6, showing a comparison of the PR EOS and the GERG-2008 EOS for the present case. In particular, it is evident from Figure 6c that PR gives a too low speed of sound at supercritical pressures below about 160 bar, and a too high speed of sound below that.

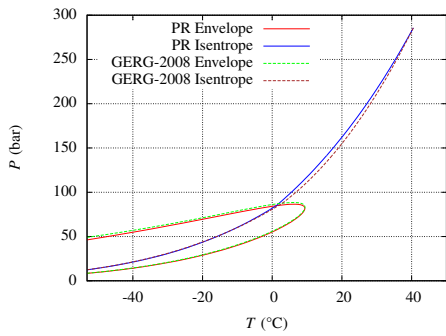
In Figure 4b, the isentropic and HEM depressurization paths for Case 2 are plotted together with the mixture phase envelope. The simulated HEM depressurization path is very close to the ideal isentropic depressurization.

3.3. Case 3: Depressurization with heat transfer

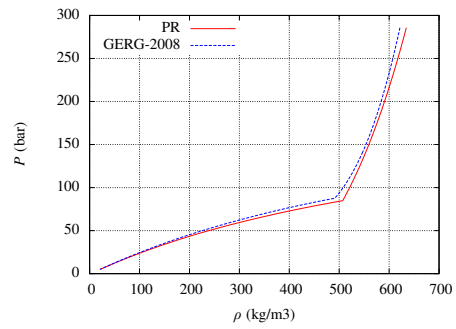
We now turn to the cases published by Drescher *et al.* (2014), which are more challenging in the sense that several closure relations are needed in the models. The depressurizations take place in a small-diameter tube and last for a long time, which imposes the necessity to model heat transfer. The long duration also makes it more challenging to capture the two-phase flow regimes encountered. Three different initial conditions and $\text{CO}_2\text{-N}_2$ mixtures are considered, see Cases 3a, 3b and 3c in Tables 1 and 2.

The test section consists of a horizontal stainless steel tube of inner diameter 10 mm and wall thickness 1 mm. The outlet valve is a manually operated ball valve, and we estimate the opening time in the equation (27) to be $t_\delta = 0.1$ s. We model the tube as straight and horizontal, with a length of 141.9 m, see Drescher *et al.* (2014). The steel has a density of 8000 kg m^{-3} , a specific heat capacity of $485 \text{ J kg}^{-1} \text{ K}^{-1}$ and a thermal conductivity of $14 \text{ W m}^{-1} \text{ K}^{-1}$. The instrument positions are given in Table 3. Further information on the test facility may be found in Pettersen *et al.* (2006); de Koeijer *et al.* (2009).

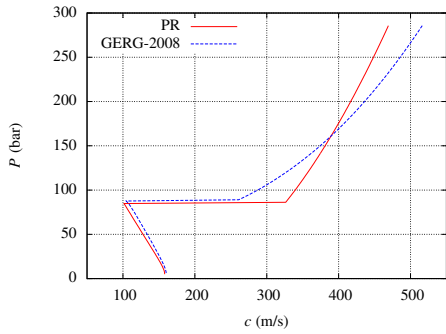
In Figure 7, the isentropic depressurization paths for Cases 3a, 3b and 3c are plotted together with the corresponding phase envelopes. For the 90 mol % case, the isentrope hits the phase envelope on the liquid side of the envelope. For the 80 mol % case, the isentrope hits very close to the critical point, while for the 70 mol % case, the isentrope hits the envelope at the gas side of the envelope. Due to the depressurization path passing very close to the critical point, the 80 mol % case is challenging to simulate. The graphs in Figure 7 also show the depressurization paths simulated using the HEM and TFM. In contrast to the preceding cases, there is a clear difference between the simulated paths and the isentropic paths. This is due to the effect of heat transfer and friction. It can be noted that the simulated paths lie between the ideal paths and the experimental observations.



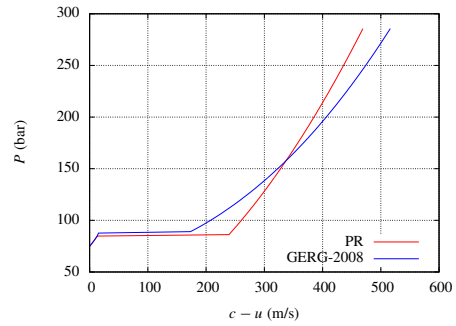
(a) Phase envelope and isentropic depressurization path.



(b) Density along isentropic depressurization path.



(c) Speed of sound along isentropic depressurization path.



(d) Ideal HEM depressurization velocity.

Figure 6: Comparison of GERG-2008 and PR for the 72.6% CO₂, 26.4% CH₄ mixture (Case 2).

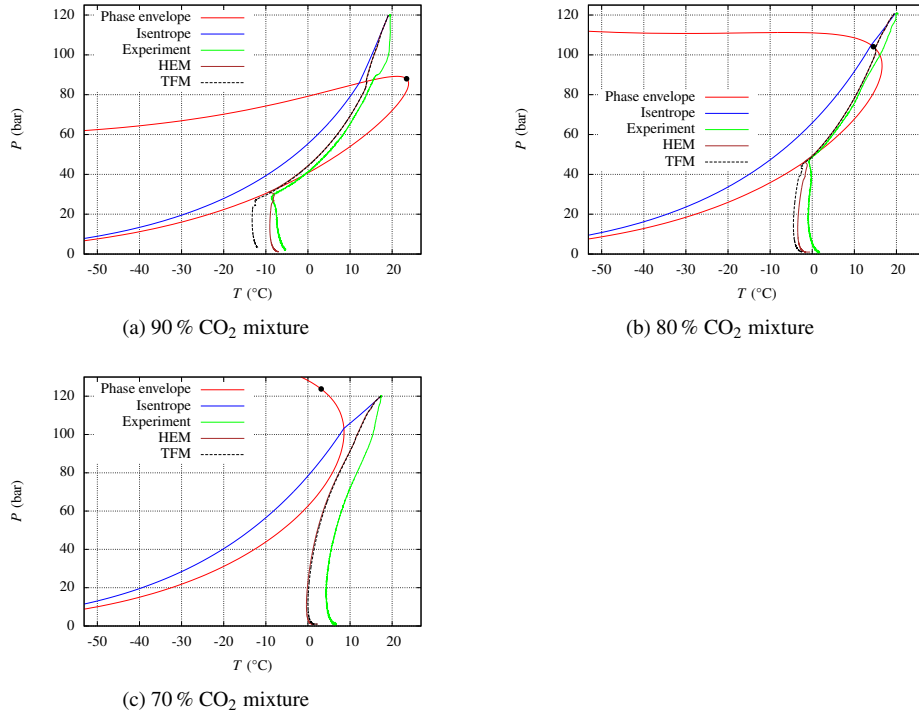


Figure 7: Case 3: Phase envelopes plotted for 90 %, 80.0 % and 70 % CO₂ together with the isentropic, experimental, HEM and TFM depressurization paths. The HEM and TFM depressurization paths are calculated using the Gungor and Winterton (1987) heat-transfer correlation. The HEM results are plotted for the PT40 position, while the experimental results are a combination of measurements from the PT40 and the TT40 positions. The critical point is plotted as a black dot, to indicate how close the depressurization path is to the critical point of the mixtures. The critical point values are also tabulated in Table 2.

For all the simulations presented in this section, unless otherwise stated, we employ the transient conduction model (23) with the Gungor and Winterton (1987) heat-transfer correlation on the inside of the tube. On the outside of the tube, we estimate a relatively high heat-transfer coefficient of $h_o = 20 \text{ W m}^{-2} \text{ K}^{-1}$ due to the occurrence of condensation.

3.3.1. Grid refinement and boundary conditions

Simulations have been run on different grids to ensure that the model equations are solved to a reasonable degree of accuracy. As an example, Figure 8a shows the temperature calculated using the HEM plotted as a function of position at time $t = 0.3 \text{ s}$. It can be seen that the difference between the grids is quite small. Henceforth, a grid of 1200 cells will be employed.

The effect of the outlet boundary condition has also been tested. The result of one such test for the HEM is plotted in Figure 8b at time $t = 0.3 \text{ s}$. The two most advanced boundary conditions, BBC and CBC described in Section 2.7, give virtually identical results. The simpler pressure BC gives too low temperatures near the outlet. However, at some distance from the outlet, the different boundary conditions give very similar results. For simplicity, we will therefore employ the pressure boundary conditions for both HEM and TFM.

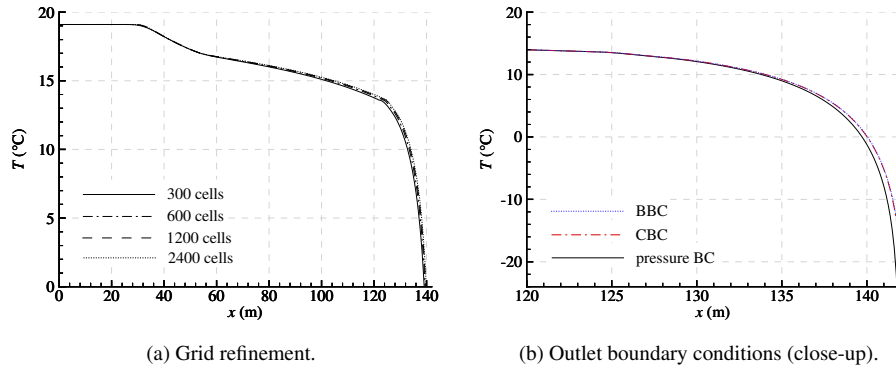


Figure 8: Case 3a, HEM: Effect of grid refinement and outlet boundary conditions on temperature at $t = 0.3$ s.

3.3.2. Comparison between HEM and TFM

Figures 9–11 compare the results obtained with the homogeneous equilibrium model (HEM) and the two-fluid model (TFM). The temperatures and pressures are plotted as a function of time at positions PT40 and TT40, respectively (about 50 m, see Table 3).

Consider now the temperatures shown in Figures 9a–11a. For 90 % CO_2 (Figure 9a), the temperature drops during 20 s to about -8°C . At this point, all the liquid has evaporated (dry-out), and the experimental data show that the temperature starts to rise. For the case of 80 % CO_2 (Figure 10a), dry-out occurs at 10 s at a temperature slightly below 0°C . For the case of 70 % CO_2 (Figure 11a), on the other hand, the state is gaseous all the time at this position, and the cooling is only due to expansion, with a minimum measured temperature of 5°C at 13 s.

Both HEM and TFM predicted the temperatures reasonably well, albeit with a tendency towards underprediction. The reason for this is mainly modelling uncertainty, although there is also an element of delay in the temperature sensors due to their thermal mass, as remarked by Drescher *et al.* (2014). This can be perceived in the initial period of about one second. For 90 % CO_2 (Figure 9), HEM predicted dry-out at about 18 s, which was two seconds early. TFM predicted dry-out at about 24 s, which was four seconds late. Initially the two models predicted very similar temperatures, with TFM slightly closer to the experimental data. After dry-out, however, TFM underpredicted the temperature to a larger degree than HEM. For 80 % CO_2 (Figure 10a), both models predicted quite similar temperatures, but TFM underpredicted the temperature more after dry-out. HEM hit the dry-out point almost spot on at about 10 s and TFM gave dry-out at 12 s. In the case of 70 % CO_2 (Figure 11a), it was TFM which gave temperatures closest to the experimental values.

We now turn to the pressures displayed in Figures 9b–11b. In general, there is good agreement between model predictions and experimental data. For 80 % CO_2 (Figure 10b), the pressure calculated by HEM is very close to the experimental values. Otherwise, there is a tendency for HEM to slightly underpredict the pressure after dry-out, with a similar tendency for TFM to overpredict the pressure (Figure 9b). For 70 % CO_2 (Figure 11b), where there is no dry-out at this position, it is the middle period which is the most difficult to predict. Here, TFM gives larger values, and HEM lower values, than the experimental data.

It should be noted that the assumption on wall friction and interfacial friction made for the TFM, using the Spedding–Hand friction correlation for stratified flow,

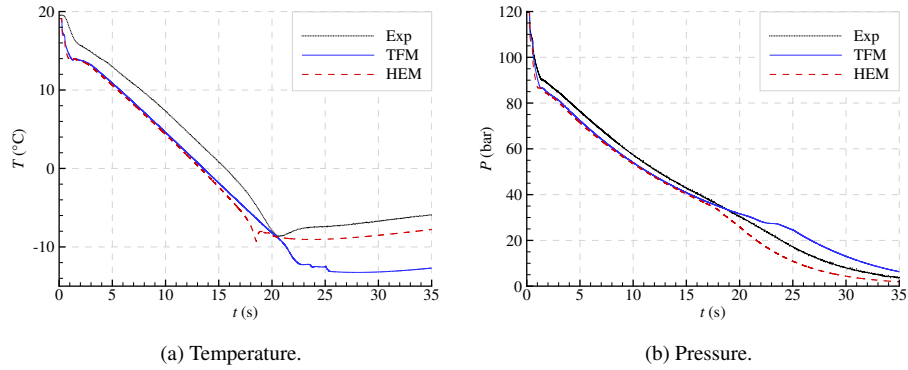


Figure 9: Case 3a, 90 % CO₂: Comparison of data from experiments (Exp), homogeneous equilibrium model (HEM) and two-fluid model (TFM) at position 50 m.

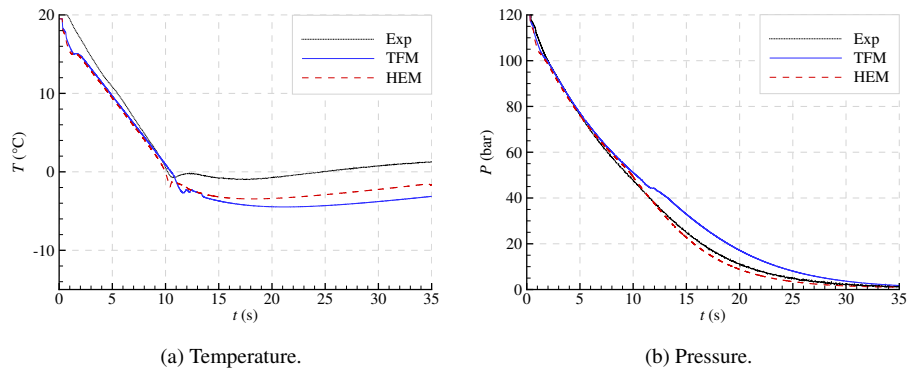


Figure 10: Case 3b, 80 % CO₂: Comparison of data from experiments (Exp), homogeneous equilibrium model (HEM) and two-fluid model (TFM) at position 50 m.

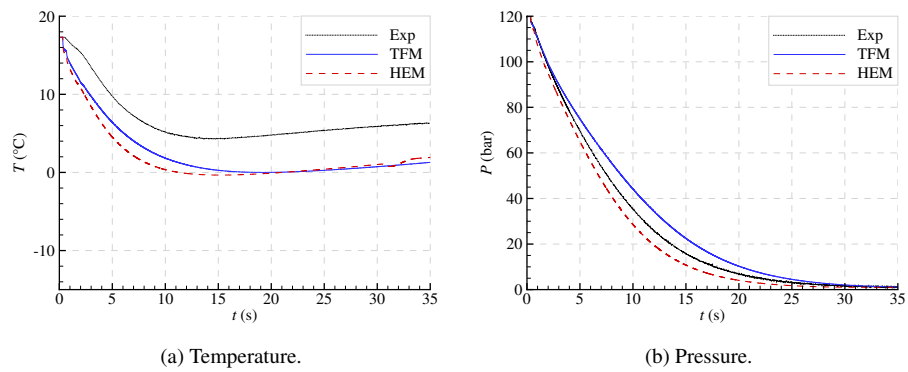


Figure 11: Case 3c, 70 % CO₂: Comparison of data from experiments (Exp), homogeneous equilibrium model (HEM) and two-fluid model (TFM) at position 50 m.

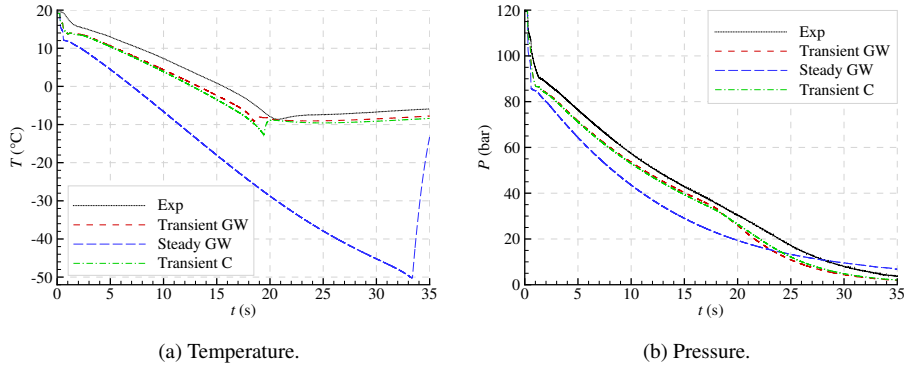


Figure 12: Case 3b, 90 % CO₂: Effect of heat-transfer models at position 50 m. HEM.

is somewhat coarse, although it is believed to be reasonable in a large part of the depressurization at some distance from the outlet. Near the outlet, the gas-liquid flow will certainly be strongly coupled, which is corroborated by the good performance of the HEM. In order to describe the actual flow, more comprehensive closure models are required. First, different flow regimes should be identified. Second, each regime should be modelled, accounting for friction, and momentum exchange through droplet entrainment/deposition to/from the gas phase. Development and validation of such models will require detailed steady-state experimental work.

3.3.3. Effect of heat-transfer modelling

The heat transfer through the tube wall has a considerable effect in this case. This is illustrated in Figure 12. The figure shows experimental data and calculations with the HEM for 90 % CO₂. In the calculations, three different models have been tested for the heat transfer. In the figure legend, ‘Transient’ denotes the transient heat equation (23), while ‘Steady’ refers to the steady-state model (22) which neglects the heat capacity of the tube. ‘GW’ denotes the Gungor and Winterton (1987) correlation for the in-tube heat-transfer coefficient, while ‘C’ denotes the simple Colburn correlation (24).

As can be seen from Figure 12a, the failure to include a transient conduction model had a profound effect on the simulated temperature. The steady model yielded far too low temperatures, -50 °C versus -10 °C, and far too late dry-out. The use of the steady conduction model also had a noticeable effect on the pressure (Figure 12b). The pressure is too low in the first part of the simulation and then too high. The result that it is necessary to include a transient conduction model is consistent with the findings of Helgaker *et al.* (2014) for single-phase flow of natural gas.

The use of an advanced (Gungor–Winterton) versus a simple (Colburn) model for the inner heat-transfer coefficient, on the other hand, had a limited effect in this case. Gungor–Winterton yielded a slightly more correct pressure before dry-out, whereas Colburn was better after dry-out. Colburn predicted the dry-out time better, but the temperature calculated using Gungor–Winterton was always closer to the experimental values. In particular, Colburn yielded a 3.5 °C lower minimum temperature.

4. Conclusion

We have presented a modelling framework to simulate two-phase flow of multicomponent CO₂-rich mixtures in pipes, discussing model predictions compared to published

data from depressurization experiments. In particular, two flow-model formulations have been tested. The first is a homogeneous equilibrium model (HEM), in which the phases travel at the same speed. The second is a two-fluid model (TFM), where the difference in phasic velocities (slip) follows from friction models. This yields the potential of including more physics. The thermodynamic properties were calculated using the Peng–Robinson equation of state (PR EOS).

The HEM was employed to simulate two cases where high-resolution pressure data were available (Cases 1 and 2). Fair agreement was obtained, both with respect to the experimental data and the 2D simulations by Elshahomi *et al.* (2015). The no-slip assumption in the HEM seems to be reasonable in these cases, where the two-phase flow is presumably strongly mixed. We hypothesize that the most significant point of improvement for further work would be to introduce a more accurate EOS. This entails some challenges associated to CPU time and the robust numerical solution of phase equilibrium for multi-term EOSs. As we illustrated for Cases 1 and 2, the GERG-2008 EOS gave significant differences compared to the PR EOS in key quantities, such as density, speed of sound and phase envelope. In the kind of computations we consider here, such differences would affect the whole result, since all the thermodynamic quantities are coupled.

Next, depressurizations of longer duration were considered, for three different CO₂-rich mixtures (Cases 3a, 3b and 3c). For cases of longer duration, the effect of heat transfer and friction becomes important. Furthermore, the cases included dry-out, which was captured reasonably well. For the inner heat-transfer coefficient, the simple Colburn correlation, and the more advanced Gungor–Winterton correlation for flow boiling, were tested. Though the latter yielded somewhat better results, only moderate sensitivity for the calculated pressure and temperature was observed. Our results clearly demonstrate, however, the necessity of considering the heat capacity of the pipe. Assuming a steady-state temperature profile in the pipe yielded far too low temperatures.

For Case 3, the HEM with the Friedel friction correlation was compared to the TFM with the Spedding–Hand friction correlation. Differences were observed in the calculations, but based on our results, we cannot say that one gives better results than the other. Regarding simplicity, the HEM is preferable. We hypothesize, however, that better results could be achieved with the TFM with specially adapted models for friction and heat transfer. The development of such models would require detailed local experimental data.

Acknowledgements

The modelling work was performed in the CO₂ Dynamics project. The authors acknowledge the support from the Research Council of Norway (189978), Gassco AS, Statoil Petroleum AS and Vattenfall AB. The reporting was carried out in the 3D Multifluid Flow project at SINTEF Energy Research. We thank Statoil for electronic access to the experimental data of Drescher *et al.* (2014). Further, thanks are due to Gelein de Koeijer and Michael Drescher of Statoil, and our colleagues Alexandre Morin and Halvor Lund, for fruitful discussions.

Kamal K. Botros of NOVA Chemicals has kindly provided the experimental data of Botros *et al.* (2013) in electronic form.

References

- Aakenes, F., Jun. 2012. *Frictional pressure-drop models for steady-state and transient two-phase flow of carbon dioxide*. Master's thesis, Department of Energy and Process Engineering, Norwegian University of Science and Technology (NTNU).
- Aakenes, F., Munkejord, S. T., Drescher, M., 2014. Frictional pressure drop for two-phase flow of carbon dioxide in a tube: Comparison between models and experimental data. *Energy Procedia* 51, 373–381. doi:10.1016/j.egypro.2014.07.044.
- Aihara, S., Misawa, K., Jul. 2010. Numerical simulation of unstable crack propagation and arrest in CO₂ pipelines. In: *The First International Forum on the Transportation of CO₂ by Pipeline*. Clarion Technical Conferences, Gateshead, UK.
- American Petroleum Institute, research project 44, 1976. *Selected values of properties of hydrocarbons and related compounds*. Thermodynamics Research Center, Texas Engineering Experiment Station, Texas A & M University, College Station, Texas, USA.
- Aursand, E., Dørum, C., Hammer, M., Morin, A., Munkejord, S. T., Nordhagen, H. O., 2014. CO₂ pipeline integrity: Comparison of a coupled fluid-structure model and uncoupled two-curve methods. *Energy Procedia* 51, 382–391. ISSN 1876-6102. doi:10.1016/j.egypro.2014.07.045.
- Aursand, P., Hammer, M., Munkejord, S. T., Wilhelmsen, Ø., Jul. 2013. Pipeline transport of CO₂ mixtures: Models for transient simulation. *Int. J. Greenh. Gas Con.* 15, 174–185. doi:10.1016/j.ijggc.2013.02.012.
- Bejan, A., 1993. *Heat Transfer*. John Wiley & Sons, Inc., New York. ISBN 0-471-50290-1.
- Bestion, D., Dec. 1990. The physical closure laws in the CATHARE code. *Nucl. Eng. Design* 124 (3), 229–245. doi:10.1016/0029-5493(90)90294-8.
- Botros, K. K., Dec. 2010. Measurements of speed of sound in lean and rich natural gas mixtures at pressures up to 37 MPa using a specialized rupture tube. *Int. J. Thermophys.* 31 (11–12), 2086–2102. doi:10.1007/s10765-010-0888-4.
- Botros, K. K., Hippert, E., Jr., Craidy, P., Jun. 2013. Measuring decompression wave speed in CO₂ mixtures by a shock tube. *Pipelines International* 16, 22–28.
- Brown, S., Martynov, S., H., M., Chen, S., Zhang, Y., 2014. Modelling the non-equilibrium two-phase flow during depressurisation of CO₂ pipelines. *Int. J. Greenh. Gas Con.* 30, 9–18. doi:10.1016/j.ijggc.2014.08.013.
- Chen, G.-Q., Toro, E. F., 2004. Centered difference schemes for non-linear hyperbolic equations. *J. Hyperbolic Differ. Equ.* 1 (3), 531–566. doi:10.1142/S0219891604000202.
- Cosham, A., Jones, D. G., Armstrong, K., Allason, D., Barnett, J., 24–28 Sep 2012. The decompression behaviour of carbon dioxide in the dense phase. In: *9th International Pipeline Conference, IPC2012*. ASME, IPTI, Calgary, Canada, vol. 3, pp. 447–464. doi:10.1115/IPC2012-90461.

- de Koeijer, G., Borch, J. H., Jakobsen, J., Drescher, M., 2009. Experiments and modeling of two-phase transient flow during CO₂ pipeline depressurization. *Energy Procedia* 1, 1649–1656. doi:10.1016/j.egypro.2009.01.220.
- Drescher, M., Varholm, K., Munkejord, S. T., Hammer, M., Held, R., de Koeijer, G., 2014. Experiments and modelling of two-phase transient flow during pipeline depressurization of CO₂ with various N₂ compositions. *Energy Procedia* 63, 2448–2457. doi:10.1016/j.egypro.2014.11.267.
- Drew, D. A., 1983. Mathematical modeling of two-phase flow. *Ann. Rev. Fluid Mech.* 15, 261–291. doi:10.1146/annurev.fl.15.010183.001401.
- Elshahomi, A., Lu, C., Michal, G., Liu, X., Godbole, A., Venton, P., 2015. Decompression wave speed in CO₂ mixtures: CFD modelling with the GERG-2008 equation of state. *Appl. Energ.* 140, 20–32. doi:10.1016/j.apenergy.2014.11.054.
- Ely, J. F., Hanley, H. J. M., Nov. 1981. Prediction of transport properties. 1. Viscosity of fluids and mixtures. *Ind. Eng. Chem. Fund.* 20 (4), 323–332. doi:10.1021/i100004a004.
- Ely, J. F., Hanley, H. J. M., Feb. 1983. Prediction of transport properties. 2. Thermal conductivity of pure fluids and mixtures. *Ind. Eng. Chem. Fund.* 22 (1), 90–97. doi:10.1021/i100009a016.
- Friedel, L., Jun. 1979. Improved friction pressure drop correlations for horizontal and vertical two phase pipe flow. In: *Proceedings, European Two Phase Flow Group Meeting*. Ispra, Italy. Paper E2.
- Gernert, J., Span, R., 2010. EOS-CG: An accurate property model for application in CCS processes. In: *Proc. Asian Thermophys. Prop. Conf.* Beijing.
- Giljarhus, K. E. T., Munkejord, S. T., Skaugen, G., 2012. Solution of the Span-Wagner equation of state using a density-energy state function for fluid-dynamic simulation of carbon dioxide. *Ind. Eng. Chem. Res.* 51 (2), 1006–1014. doi:10.1021/ie201748a.
- Gungor, K. E., Winterton, R. H. S., Mar. 1987. Simplified general correlation for saturated flow boiling and comparisons of correlations with data. *Chem. Eng. Res. Des.* 65 (2), 148–156.
- Hammer, M., Ervik, Å., Munkejord, S. T., 2013. Method using a density-energy state function with a reference equation of state for fluid-dynamics simulation of vapor-liquid-solid carbon dioxide. *Ind. Eng. Chem. Res.* 52 (29), 9965–9978. doi:10.1021/ie303516m.
- Hammer, M., Morin, A., Sep. 2014. A method for simulating two-phase pipe flow with real equations of state. *Comput. Fluids* 100, 45–58. doi:10.1016/j.compfluid.2014.04.030.
- Helgaker, J. F., Oosterkamp, A., Langelandsvik, L. I., Ytrehus, T., 2014. Validation of 1D flow model for high pressure offshore natural gas pipelines. *J. Nat. Gas Sci. Eng.* 16, 44–56. doi:10.1016/j.jngse.2013.11.001.
- Hetland, J., Barnett, J., Read, A., Zapatero, J., Veltin, J., 2014. CO₂ transport systems development: Status of three large European CCS demonstration projects with EEPR funding. *Energy Procedia* 63, 2458–2466. doi:10.1016/j.egypro.2014.11.268.

- IEA, 2014. *Energy Technology Perspectives*. ISBN 978-92-64-20801-8. doi:10.1787/energy_tech-2014-en.
- Jie, H. E., Xu, B. P., Wen, J. X., Cooper, R., Barnett, J., Sep. 2012. Predicting the decompression characteristics of carbon dioxide using computational fluid dynamics. In: *9th International Pipeline Conference IPC2012*. ASME, IPTI, Calgary, Canada, pp. 585–595. ISBN 978-0-7918-4514-1. doi:10.1115/IPC2012-90649.
- Jones, D. G., Cosham, A., Armstrong, K., Barnett, J., Cooper, R., Oct. 2013. Fracture-propagation control in dense-phase CO₂ pipelines. In: *6th International Pipeline Technology Conference*. Lab. Soete and Tiratsoo Technical, Ostend, Belgium. Paper no. S06-02.
- Klinkby, L., Nielsen, C. M., Krogh, E., Smith, I. E., Palm, B., Bernstone, C., 2011. Simulating rapidly fluctuating CO₂ flow into the vedsted CO₂ pipeline, injection well and reservoir. *Energy Procedia* 4, 4291–4298. doi:10.1016/j.egypro.2011.02.379.
- Kunick, M., Kretzschmar, H.-J., Gampe, U., Sep. 2008. Fast calculation of thermodynamic properties of water and steam in process modelling using spline interpolation. In: *Proceedings 15th International Conference on the Properties of Water and Steam, ICPWS XV*. Berlin, Germany.
- Kunz, O., Wagner, W., October 2012. The GERG-2008 wide-range equation of state for natural gases and other mixtures: An expansion of GERG-2004. *J. Chem. Eng. Data* 57 (11), 3032–3091. doi:10.1021/jc300655b.
- Li, H., Jakobsen, J. P., Wilhelmsen, Ø., Yan, J., Nov. 2011a. PVT_{xy} properties of CO₂ mixtures relevant for CO₂ capture, transport and storage: Review of available experimental data and theoretical models. *Appl. Energ.* 88 (11), 3567–3579. doi:10.1016/j.apenergy.2011.03.052.
- Li, H., Wilhelmsen, Ø., Lv, Y., Wang, W., Yan, J., Sep. 2011b. Viscosity, thermal conductivity and diffusion coefficients of CO₂ mixtures: Review of experimental data and theoretical models. *Int. J. Greenh. Gas Con.* 5 (5), 1119–1139. doi:10.1016/j.ijggc.2011.07.009.
- Liou, M.-S., Steffen, C. J., Jr., 1993. A new flux splitting scheme. *J. Comput. Phys.* 107 (1), 23–39. doi:10.1006/jcph.1993.1122.
- Mahgerefteh, H., Brown, S., Denton, G., May 2012. Modelling the impact of stream impurities on ductile fractures in CO₂ pipelines. *Chem. Eng. Sci.* 74, 200–210. doi:10.1016/j.ces.2012.02.037.
- Michelsen, M. L., 1999. State function based flash specifications. *Fluid Phase Equilib.* 158-160, 617–626. doi:10.1016/S0378-3812(99)00092-8.
- Michelsen, M. L., Mollerup, J. M., 2007. *Thermodynamic models: Fundamentals & computational aspects*. Tie-Line Publications, Holte, Denmark, second ed. ISBN 87-989961-3-4.
- Morin, A., Flåtten, T., 2012. A two-fluid four-equation model with instantaneous thermodynamical equilibrium. *Submitted URL* <http://www.stat.ntnu.no/conservation/2013/002.pdf>.

- Munkejord, S. T., Jul. 2006. Partially-reflecting boundary conditions for transient two-phase flow. *Commun. Numer. Meth. En.* 22 (7), 781–795. doi:10.1002/cnm.849.
- Munkejord, S. T., Bernstone, C., Clausen, S., de Koeijer, G., Mølnvik, M. J., 2013. Combining thermodynamic and fluid flow modelling for CO₂ flow assurance. *Energy Procedia* 63, 2904–2913. doi:10.1016/j.egypro.2013.06.176.
- Munkejord, S. T., Evje, S., Flåtten, T., Oct. 2006. The multi-stage centred-scheme approach applied to a drift-flux two-phase flow model. *Int. J. Numer. Meth. Fl.* 52 (6), 679–705. doi:10.1002/flid.1200.
- Munkejord, S. T., Evje, S., Flåtten, T., Jun. 2009. A MUSTA scheme for a nonconservative two-fluid model. *SIAM J. Sci. Comput.* 31 (4), 2587–2622. doi:10.1137/080719273.
- Munkejord, S. T., Jakobsen, J. P., Austegard, A., Mølnvik, M. J., Jul. 2010. Thermo- and fluid-dynamical modelling of two-phase multi-component carbon dioxide mixtures. *Int. J. Greenh. Gas Con.* 4 (4), 589–596. doi:10.1016/j.ijggc.2010.02.003.
- NETL, Aug. 2013. *CO₂ impurity design parameters*. Tech. Rep. DOE/NETL-341-011212, National Energy Technology Laboratory, USA.
- Nordhagen, H. O., Kragset, S., Berstad, T., Morin, A., Dørum, C., Munkejord, S. T., Mar. 2012. A new coupled fluid-structure modelling methodology for running ductile fracture. *Comput. Struct.* 94–95, 13–21. doi:10.1016/j.compstruc.2012.01.004.
- Paillère, H., Corre, C., García Cascales, J. R., Jul. 2003. On the extension of the AUSM+ scheme to compressible two-fluid models. *Comput. Fluids* 32 (6), 891–916. doi:10.1016/S0045-7930(02)00021-X.
- Peng, D. Y., Robinson, D. B., Feb. 1976. A new two-constant equation of state. *Ind. Eng. Chem. Fund.* 15 (1), 59–64. doi:10.1021/i160057a011.
- Pettersen, J., de Koeijer, G., Hafner, A., Jun. 2006. Construction of a CO₂ pipeline test rig for R&D and operator training. In: *GHGT-8 – 8th International Conference on Greenhouse Gas Control Technologies*. Trondheim, Norway.
- Pini, M., Spinelli, A., Persico, G., Rebay, S., 2015. Consistent look-up table interpolation method for real-gas flow simulations. *Comput. Fluids* 107, 178–188. doi:10.1016/j.compfluid.2014.11.001.
- Spedding, P. L., Hand, N. P., 1997. Prediction in stratified gas-liquid co-current flow in horizontal pipelines. *Int. J. Heat Mass Tran.* 40 (8), 1923–1935. doi:10.1016/S0017-9310(96)00252-9.
- Stryjek, R., Vera, J. H., 1986. PRSV: An improved Peng–Robinson equation of state for pure compounds and mixtures. *Can. J. Chem. Eng.* 64 (2), 323–333. doi:10.1002/cjce.5450640224.
- Stuhmiller, J. H., Dec. 1977. The influence of interfacial pressure forces on the character of two-phase flow model equations. *Int. J. Multiphase Flow* 3 (6), 551–560. doi:10.1016/0301-9322(77)90029-5.
- Swesty, F., 1996. Thermodynamically consistent interpolation for equation of state tables. *J. Comput. Phys.* 127 (1), 118–127. doi:10.1006/jcph.1996.0162.

- Timmes, F. X., Swesty, F. D., 2000. The accuracy, consistency, and speed of an electron-positron equation of state based on table interpolation of the Helmholtz free energy. *Astrophys. J. Suppl. S.* 126 (2), 501–516. doi:10.1086/313304.
- Titarev, V. A., Toro, E. F., Sep. 2005. MUSTA schemes for multi-dimensional hyperbolic systems: analysis and improvements. *Int. J. Numer. Meth. Fl.* 49 (2), 117–147. doi:10.1002/flid.980.
- Toro, E. F., Oct.–Nov. 2006. MUSTA: A multi-stage numerical flux. *Appl. Numer. Math.* 56 (10–11), 1464–1479. doi:10.1016/j.apnum.2006.03.022.
- Toro, E. F., Billett, S. J., Nov. 2000. Centred TVD schemes for hyperbolic conservation laws. *IMA J. Numer. Anal.* 20 (1), 47–79. doi:10.1093/imanum/20.1.47.
- US DOE, 2010. *Interagency Task Force on Carbon Capture and Storage*. Washington, DC, USA.
- Wareing, C. J., Fairweather, M., Falle, S. A. E. G., Woolley, R. M., 2014. Validation of a model of gas and dense phase CO₂ jet releases for carbon capture and storage application. *Int. J. Greenh. Gas Con.* 20, 254–271. doi:10.1016/j.ijggc.2013.11.012.
- Xia, G., Li, D., Merkle, C. L., 2007. Consistent properties reconstruction on adaptive cartesian meshes for complex fluids computations. *J. Comput. Phys.* 225 (1), 1175–1197. doi:10.1016/j.jcp.2007.01.034.
- Xu, B. P., Jie, H. E., Wen, J. X., 2014. A pipeline depressurization model for fast decompression and slow blowdown. *Int. J. Pres. Ves. Pip.* 123–124, 60–69. doi:10.1016/j.ijpvp.2014.07.003.